

Investigating a fluctuating-accretion model for the spectral-timing properties of accreting black hole systems

P. Arévalo¹[★] and P. Uttley²

¹Max-Planck-Institut für Extraterrestrische Physik, Postfach 1312, D-85741 Garching, Germany

²NASA Goddard Space Flight Center, Greenbelt, MD 20771, USA

Accepted 2005 December 14. Received 2005 December 9; in original form 2005 September 26

ABSTRACT

The fluctuating-accretion model of Lyubarskii and its extension by Kotov, Churazov & Gilfanov seek to explain the spectral-timing properties of the X-ray variability of accreting black holes in terms of inward-propagating mass accretion fluctuations produced at a broad range of radii. The fluctuations modulate the X-ray emitting region as they move inwards and can produce temporal-frequency-dependent lags between energy bands, and energy-dependent power spectral densities (PSDs) as a result of the different emissivity profiles, which may be expected at different X-ray energies. Here, we use a simple numerical implementation to investigate in detail the X-ray spectral-timing properties of the model and their relation to several physically interesting parameters, namely the emissivity profile in different energy bands, the geometrical thickness and viscosity parameter of the accretion flow, the strength of damping on the fluctuations and the temporal coherence (measured by the ‘quality factor’, Q) of the fluctuations introduced at each radius. We find that a geometrically thick flow with large viscosity parameter is favoured, and we confirm that the predicted lags are quite robust to changes in the emissivity profile and physical parameters of the accretion flow, which may help to explain the similarity of the lag spectra in the low/hard and high/soft states of Cyg X-1. We also demonstrate the model regime where the light curves in different energy bands are highly spectrally coherent. We compare model predictions directly to X-ray data from the narrow line Seyfert 1 galaxy NGC 4051 and the black hole X-ray binary (BHXRB) Cyg X-1 in its high/soft state, and we show that this general scheme can reproduce simultaneously the time lags and energy-dependence of the PSD.

Key words: accretion, accretion discs – galaxies: active.

1 INTRODUCTION

A common characteristic in active galactic nuclei (AGN) and X-ray binary systems (XRBs) is their strongly variable X-ray emission. Most of the variability power is in the form of aperiodic fluctuations that span several orders of magnitude in temporal frequency (e.g. van der Klis 1995; McHardy et al. 2004). Rapid, large amplitude X-ray variations, on time-scales down to milliseconds in XRBs and minutes in AGN, are commonly observed (e.g. Revnivtsev, Gilfanov & Churazov 2000; Gierliński & Zdziarski 2003; McHardy et al. 2004), supporting the expectation from accretion theory that the bulk of the emission must originate close to the central black hole. However, in many sources (in both AGN and XRBs), large-amplitude X-ray variations, of tens of per cent fractional rms, are observed over several decades of time-scales (e.g. Reig, Papadakis & Kylafis 2002;

McHardy et al. 2004; Uttley & McHardy 2005), including values orders of magnitude longer than the viscous time-scale of the inner disc, suggesting that these fluctuations must originate at large radii. This discrepancy motivated the appearance of propagating-fluctuation models, as proposed by Lyubarskii (1997), who noted that while the *emission* might be produced only in the innermost regions, the *variability* can originate throughout the accretion flow. In this model, accretion rate fluctuations arise over a wide range of radii and, correspondingly, a wide range of time-scales, and they propagate inwards to modulate the central X-ray emission.

As noted by Uttley & McHardy (2001), the model of Lyubarskii (1997) is consistent with the observed linear relation between rms-variability amplitude and mean count rate in XRB and AGN X-ray light curves, which implies a coupling between fluctuations on different time-scales, ruling out models where the variability arises from strictly independent flares or active regions (Uttley, McHardy & Vaughan 2005). Fluctuating-accretion models, on the other hand, are consistent with this relation: the fluctuations couple together

[★]E-mail: parevalo@mpe.mpg.de

as they propagate down to the centre, so low-frequency fluctuations produced at large radii modulate higher-frequency fluctuations produced further in. A linear rms–flux relation is also observed in neutron star XRB systems, where the emission mechanism is most likely different to the one operating in black hole systems (Uttley & McHardy 2001; Uttley 2004). This result provides additional evidence for fluctuating-accretion scenarios because it suggests that the variability originates in the accretion flow and not just locally via the mechanism producing the emission (Uttley 2004).

Besides explaining the broad range of variability time-scales and the rms–flux relation, the fluctuating-accretion model can also explain the spectral-timing properties of the variability, as noted by Kotov, Churazov & Gilfanov (2001). For example, it has long been known (e.g. Miyamoto & Kitamoto 1989; Nowak, Wilms & Dove 1999a) that X-ray variations in black hole X-ray binaries (BHXBs) often show hard lags, i.e. a delay in hard X-ray variations with respect to soft X-rays, which is larger for variations on longer time-scales, and at higher energies. The magnitudes of the lags are typically of order 1 per cent of the variability time-scale. Similar time-scale-dependent, hard lags have recently been discovered in AGN, albeit on much longer time-scales, commensurate with their higher black hole masses (e.g. Papadakis, Nandra & Kazanas 2001; Vaughan, Fabian & Nandra 2003; McHardy et al. 2004). In their analytical extension to Lyubarskii’s model, Kotov et al. (2001) explain these lags by invoking a radially extended X-ray emitting region with an energy-dependent profile. In this scenario, the response of the emission to a fluctuation in the accretion flow is a function of the inward propagation time-scale and hence radius of the origin, of the fluctuation, combined with the emissivity profile. Hence, if the emissivity profile is more centrally concentrated at higher energies, hard-band lags are produced such that the lags are larger for longer time-scale variations. Kotov et al. (2001) show that the same basic picture can also explain the energy dependence of the power spectral density (PSD) of BHXBs and AGN, where there is relatively more high-frequency power observed at higher energies than at lower energies (e.g. Nowak et al. 1999b; McHardy et al. 2004). This is because the emitting region acts as a low-pass filter and, as the emitting region of the soft band is more extended, the higher-frequency variations are filtered more strongly in the soft band.

Due to its success in explaining many aspects of the X-ray variability data, the fluctuating-accretion model of Lyubarskii (1997) and Kotov et al. (2001) warrants a deeper investigation, which is the aim of this paper. As shown by the brief analytical treatment of Kotov et al. (2001), in principle, the model produces time-scale-dependent lags of approximately the same amplitude as observed in the data, and energy-dependent PSDs. However, it is not clear exactly how the lag spectrum (lag as a function of Fourier frequency) and energy dependence of the PSD varies as a function of emissivity profile, or the parameters of the accretion flow (assuming the standard disc model of Shakura & Sunyaev 1973, e.g. the viscosity parameter α or the scaleheight of the flow), or due to the effects of radial damping of variations in the accretion flow. Furthermore, because Kotov et al. (2001) analytically determined spectral-timing properties by making the simplifying assumption that the perturbation introduced into the accretion flow at each radius is a delta function in time and radius, it is important to determine the effects on spectral-timing properties of a more realistic model, where stochastic variations over a broader range of time-scales are introduced at each radius. Finally, the fluctuating-accretion model should, in principle, produce light curves that are highly correlated in different bands (i.e. spectrally coherent, see Vaughan & Nowak 1997 and Appendix B of

this paper), but this aspect of the model has not yet been studied. To study these various effects in more detail, in Section 2 we introduce a computational toy model for a fluctuating accretion flow, based on the work of Lyubarskii (1997) and Kotov et al. (2001), and we explore the dependence of the PSD, time lags and coherence on the model parameters in Section 3. We show how the model predictions fit X-ray data from AGN and the BHXB Cyg X-1 in Sections 4 and 5. Specifically, we will concentrate on explaining the spectral-timing properties of the BHXB Cyg X-1 in its high/soft state and AGN that show similar variability properties, because these states show rather simple $1/f$ -type PSD shapes, without complex quasi-periodic oscillations (QPOs). We discuss the implications of our results in Section 6 and summarize our results in Section 7.

2 THE MODEL

2.1 Model construction and basic assumptions

The model is based on the scenario proposed by Lyubarskii (1997), where fluctuations propagate inwards through the accretion flow, modulating the emission of the inner regions. The fluctuations are produced on time-scales related to the viscous time-scale at the radius of origin and are uncorrelated for different radial scales. Churazov, Gilfanov & Revnivtsev (2001) noted that, in this class of models, the accretion rate fluctuations can be carried efficiently and be produced up to high Fourier frequencies, by a geometrically thick accretion flow, identifying it with an extended corona over the thin disc.

We use standard accretion disc (Shakura & Sunyaev 1973) considerations to relate the fluctuation time-scales and propagation speeds to the radial position in the disc, because the same relations are applicable to geometrically thick and optically thin accretion flows, as well as the standard geometrically thin disc. Following Lyubarskii (1997), we assume that each independent annulus produces a pattern of fluctuations $\dot{m}(r, t)$, having most of the variability power at the local viscous frequency $f_{\text{visc}}(r) = r^{-3/2}(H/R)^2\alpha/2\pi$ (e.g. Kato, Fukue & Mineshige 1998), where (H/R) is the disc scale-height to radius ratio, α is the viscosity parameter, the radial position r is in units of gravitational radii $R_g = GM/c^2$ and the frequency is given in terms of c/R_g . The local accretion rate at any radius in the disc is allowed to fluctuate around a value $\dot{M}_o(r, t)$, as $\dot{M}(r, t) = \dot{M}_o(r, t) \times [1 + \dot{m}(r, t)]$, where $\dot{m}(r, t) \ll 1$. As this new value of the accretion rate propagates inwards, it serves as the $\dot{M}_o(r, t)$ for the fluctuations produced further in, modulating the higher-frequency fluctuations. The propagation speed is assumed to equal the local radial drift velocity $v_{\text{visc}}(r) = r^{-1/2}(H/R)^2\alpha$.

A key feature of this model is that the absolute amplitude of accretion rate variations is proportional to the local accretion rate, $\dot{M}_o(r, t)$, at every radius. Considering that the characteristic frequencies of the input fluctuation $\dot{m}(r, t)$ decrease with radius, this implies that the amplitude of high-frequency fluctuations is proportional to the actual value of the accretion rate, given by fluctuations on longer time-scales, and this produces the rms–flux relation.

To generate light curves, following Kotov et al. (2001), we assume that the X-rays are emitted by a radially (but not necessarily vertically) extended region. This emitting region might correspond to an accreting corona, possibly sandwiching an optically thick, geometrically thin disc, or be another type of optically thin accretion flow [e.g. advection-dominated accretion flow (ADAF), Narayan & Yi 1994]. Having no pre-defined emission mechanism, we simply assume that the emitted flux per unit area is proportional to the local accretion rate, which introduces the variability, and to a

stable radial emissivity profile. The emissivity profile, $\epsilon(r)$, is taken to follow the radial rate of gravitational energy loss in the accretion disc, $\epsilon(r) = r^{-3}(1 - \sqrt{r_{\min}/r})$, where r_{\min} is the inner radius of the disc (and of the emission), which we will fix at $6R_g$ in our simulations. This profile describes the *total* energy loss. However, as the emitted spectrum might be radially dependent, a given energy band can have a different emissivity profile and so we will use $\epsilon(r) = r^{-\gamma}(1 - \sqrt{r_{\min}/r})$, where the emissivity index γ is a model parameter.

2.2 Numerical implementation

For the calculation of the variability patterns, we discretize the models of Lyubarskii (1997) and Kotov et al. (2001) by assuming that a finite number of annuli produce independent fluctuations. These annuli are spaced keeping a constant ratio between consecutive radii, to mimic the behaviour of a continuous accretion flow that produces equal variability power at each radial scale. This geometric spacing of the radii introduces equal power per decade in time-scale, reproducing the $1/f$ PSD shape, as predicted by Lyubarskii (1997).

All these independent annuli are assumed to produce a pattern of small accretion rate fluctuations, $\dot{m}(r, t)$. To meet the requirement of producing most of the variability power at the viscous frequency, these signals are modelled as random fluctuations with a Lorentzian-shaped PSD of variable width, with peak frequency f_{peak} .¹ The width of the Lorentzian is governed by the quality factor Q , equal to the ratio of Lorentzian peak frequency to the full width at half maximum. We used broad input PSDs, with $Q = 0.5$, a value similar to the four-Lorentzian decomposition of the PSD of Cyg X-1 in the low/hard state (Pottschmidt et al. 2003), and also much narrower PSDs with $Q = 10$, to study the influence of these parameters on the final PSDs and cross-spectra. The normalization of these signal PSDs was chosen to produce a final fractional variability of the output light curves $F_{\text{var}} \sim 10\text{--}50$ per cent, by assigning each of the signals an rms $\sigma_{\text{sig}} = \sqrt{F_{\text{var}}^2/N}$, where $N \sim 1000$ is the number of independent annuli. We used the method described by Timmer & König (1995) to generate the signal time series $\dot{m}(r, t)$, i.e. by generating periodograms with the underlying signal PSD and the correct statistical properties of a noise process and obtaining $\dot{m}(r, t)$ through their inverse Fourier transform. The resulting $\dot{m}(r, t)$ have zero mean and rms amplitude $\sim \sigma_{\text{sig}} \ll 1$.

The accretion rate at a given annulus, $\dot{M}(r_i, t)$, is then calculated iteratively as the product of the accretion rate at that position, including its contribution to the fluctuation, $1 + \dot{m}(r_i, t)$, by the accretion rate at the annulus lying directly outside, which includes the fluctuations from all outer annuli,

$$\dot{M}(r_i, t) = \dot{M}_0 \prod_{j=0}^i (1 + \dot{m}(r_j, t)), \quad (1)$$

so that each $\dot{M}(r_i, t)$ is a flicker noise time series with power-law PSD of slope ~ -1 up to $f_{\text{visc}}(r_i)$ and shows a linear rms–flux relation.

The effect of the extended emitting region is accounted for when calculating the *light curves*. First, an emissivity index γ is assumed for each energy band. Then, the light curves are constructed by adding the variability patterns $\dot{M}(r_i, t)$ from all annuli, which are

¹ The Lorentzian peak frequency corresponds to the frequency where the contribution to total rms is at its maximum, and it is related to the resonance or centroid frequency f_{centroid} as $f_{\text{peak}} = f_{\text{centroid}} \sqrt{1 + 1/4Q^2}$ (e.g. see Pottschmidt et al. 2003) set to equal f_{visc} .

weighted by the flux originating from each annulus [i.e. $2\pi r \delta r \epsilon(r)$, where δr is the width of the annulus], and time-shifted by the propagation time of fluctuations from the outermost annulus to the present annulus.

The disc parameters are either kept constant or allowed to vary radially as $(H/R)^2 \alpha(r) = Cr^{-\beta}$, where C is a scaling constant and β is an index that governs the radial variation (e.g. constant H/R and α correspond to $\beta = 0$). We will normally use $C = 0.3 \times 6.0^\beta$, to produce thick disc parameters $(H/R)^2 = 1$ and $\alpha = 0.3$ at the innermost radius. Radially varying disc parameters change the radial separation of independent annuli but preserve the separation of independent characteristic frequencies. Therefore, we fix the geometrically spaced frequencies and use $(H/R)^2 \alpha(r)$ to calculate the corresponding radii and propagation speeds.

Fig. 1 shows a light-curve realization with emissivity index $\gamma = 3$ (Fig. 1a), together with its PSD, plotted as frequency multiplied by power (Fig. 1b), and its rms variability amplitude plotted versus the average count rate of short sections of the light curve (Fig. 1c).

Finally, damping of the fluctuations as they propagate through the accretion flow affects the power spectra of the transmitted signals. The magnitude of the damping effect depends on the nature of the fluctuations and their propagation mechanism, which are not specified in our phenomenological model. In their analytical model, Kotov et al. (2001) include this damping effect by using a Green function for diffusion in the geometrically thin disc approximation. Here, for simplicity and generality, we use a simple prescription for damping by assuming that fluctuations of frequency f are significantly damped after travelling a distance $\Delta r/r = \sqrt{f_{\text{visc}}(r)/f}$, so that fluctuations on frequencies much higher than the local viscous frequency are strongly suppressed (see, for example, Churazov et al. 2001, but notice that in that case damping was

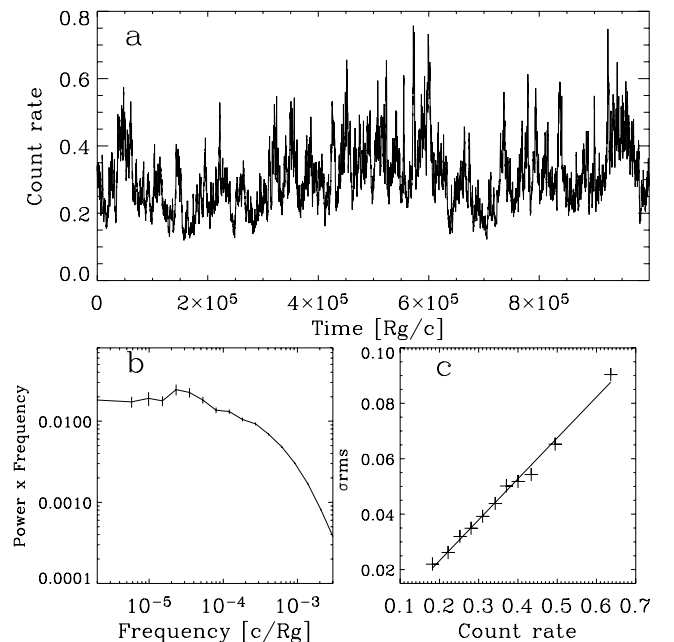


Figure 1. (a) Light curve from a realization of the variability model, with emissivity index $\gamma = 3$. (b) PSD of the same light curve, here plotted as power \times frequency, showing the typical $1/f$ shape at low frequencies [i.e. a flat top in this representation, which shows the relative contribution of rms from each decadal range in frequency, analogous to the $\nu F(\nu)$ form of a spectral energy distribution (SED)]. The PSD bends to steeper slopes towards $f_{\text{visc}}(r_{\min}) = 3 \times 10^{-3} c/R_g$. (c) σ_{rms} versus flux for the same light curve, showing a linear relation.

specifically derived for diffusive propagation of a delta-function shaped impulse in mass accretion rate). The damping prescription is implemented by first taking the Fourier transform of $\dot{M}(r_i, t)$ at each radial step r_i , then multiplying the real and imaginary coefficients of the Fourier transform at each frequency f by a frequency-dependent factor $\exp[-D(\Delta r/r_i)\sqrt{f/f_{\text{visc}}(r_i)}]$ (where the damping coefficient D is a free parameter) and inverse Fourier-transforming the result to get the new, damped $\dot{M}(r_i, t)$.

Throughout this paper, we will use $R_g = GM/c^2$ as units of distance and R_g/c as units of time. For a quick check of frequencies and time-scales, note that $R_g/c \sim (5M/M_6)$ s where $M_6 = 10^6 M_\odot$, so the frequencies quoted would be in units of Hz for a $2 \times 10^5 M_\odot$ black hole and units of 10^4 Hz for a $20 M_\odot$ black hole.

2.3 Analytical estimates

The extended emitting region acts as a low-pass filter on the PSD. This effect can be understood by considering that the signals at low temporal frequencies are imprinted in the flux from most of the emitting region, while higher frequencies are only imprinted in the emission from smaller, inner areas. As the light curve has additive components from all these regions, this produces comparatively less variability power at high frequencies, creating a bend in the PSD. The ‘filtered’ PSD can be approximated by multiplying the original PSD(f) by the squared fraction of the total flux that is produced within the characteristic radius r_f of each frequency f as

$$\text{PSD}_{\text{filt}}(f) = \text{PSD}(f) \left[\frac{\int_{r_{\min}}^{r_f} \epsilon(r) 2\pi r dr}{\int_{r_{\min}}^{\infty} \epsilon(r) 2\pi r dr} \right]^2. \quad (2)$$

The filter factor tends to 1 as r_f tends to ∞ , i.e. for low temporal frequencies the original variability power is preserved, and decreases monotonically as r_f reaches r_{\min} , reducing the variability power at the high-frequency end. Obviously, as the emissivity profiles $\epsilon(r)$ used are steep, it makes little difference to the filtered PSD if the emission region is truncated at a large radius rather than extending to infinity.

The filtering effect due to the origin of the signals within the emitting region could be easily calculated once the emissivity profile is defined, and its effect is simply to reduce the overall *normalization* of the contribution to the PSD from each signal (in a frequency-dependent way), without distorting the signal PSD shape. However, the finite traveltime of the fluctuations through the emitting region distorts the PSD shape of the input signals, by smoothing out high-frequency fluctuations, thus reducing the variability amplitude further, while damping can also affect the low-frequency power. Therefore, the total effective filtering of the underlying fluctuations is quite complex, so we will primarily use numerical simulations to demonstrate its effects in the following section.

The frequency-resolved time lags can be approximated by defining, for each signal s (produced at radius r_s), an ‘average traveltime’, $\bar{\tau}(r_s)$, by weighting the traveltime of the fluctuations from r_s to the radius r , $\tau(r, r_s)$ by the emissivity profile $\epsilon(r)$,

$$\bar{\tau}(r_s) = \frac{\int_{r_{\min}}^{r_s} \tau(r, r_s) \epsilon(r) 2\pi r dr}{\int_{r_{\min}}^{r_s} \epsilon(r) 2\pi r dr}, \quad (3)$$

$$\text{where } \tau(r, r_s) = \int_r^{r_s} \frac{d\bar{r}}{v_{\text{visc}}(\bar{r})}.$$

If the signals are simple fluctuations on the viscous time-scale only (i.e. defined by a delta function and not a broad Lorentzian PSD), then r_s can be expressed in terms of frequency and this formula gives the mean traveltime as a function of f . Otherwise, if the

signals are characterized by broad Lorentzian PSDs, a given temporal frequency will have important contributions from a range in radii r_s . In this case, the mean traveltime at a given frequency f is a sum of $\bar{\tau}$ for each contributing (i.e. overlapping) Lorentzian signal PSD, weighted by the variability power at f contributed by that signal.

Time lags between two energy bands appear when they are characterized by different emissivity indices, because this produces different mean traveltimes for each band. We will use the difference of $\bar{\tau}(f)$ calculated with the corresponding γ indices as an approximation of the time lags between energy bands.

An explicit form for the filter factor of the PSD and for the time lags is given in Appendix A.

3 SPECTRAL-TIMING PROPERTIES

The model was constructed to produce power-law-PSD time series that also reproduce the non-linear properties of AGN and BHXRB light curves. The exact PSD shape and spectral-timing properties between different energy bands depend on a few key model parameters: emissivity indices, disc structure parameters, the PSD of the input signals and the damping coefficient. Here, we will explore how each of these parameters affects the observable properties. An overview of the spectral-timing measurements we use here is provided in Appendix B.

3.1 Dependence on emissivity indices

The loss of gravitational energy in the accretion disc requires an energy release per unit area proportional to $\epsilon(r) = r^{-3}(1 - \sqrt{r_{\min}/r})$ (Shakura & Sunyaev 1973). A given energy band will have the same radial emissivity profile only if it represents a constant fraction of the emitted flux at each radius. However, following Kotov et al. (2001), we assume the emitted spectrum hardens towards the centre, so the actual radial emissivity profile will be steeper for harder bands. We will refer to time series constructed with emissivity index $\gamma = 3$ as the ‘soft’ light curve and use higher values of γ for the ‘hard’ bands. In this subsection, we assume the product of disc structure parameters $(H/R)^2 \alpha = 0.3$ and that there is no damping ($D = 0$).

The PSD of the final variability pattern at r_{\min} for a realization with input signal $Q = 0.5$ is shown by the solid line in Fig. 2. This PSD would correspond to an infinitely concentrated emitting region located at r_{\min} , or equivalently, a compact emitting region located entirely *within* r_{\min} . It keeps a $1/f$ behaviour (corresponding to a flat top in this plot of power multiplied by frequency) up to $f_{\text{visc}}(r_{\min}) = 3 \times 10^{-3} c/R_g$ and, as no annuli contribute with significant variability power above this frequency, the PSD bends downwards. The dotted and dashed lines show the PSDs of soft and hard light curves from a realization with the same underlying accretion fluctuations, with $\gamma_{\text{soft}} = 3$ and $\gamma_{\text{hard}} = 5$, respectively. The figure highlights the filtering effect of the extended emission on these two light curves, which makes them lose variability power at high frequencies, shifting the bend to lower frequencies. On longer time-scales, all the PSDs flatten to their original slope of -1 . The resulting PSDs bend continuously to steeper slopes at high frequencies but, for a limited frequency range, they can be approximated fairly well by a singly bending power-law model, as has been used to fit real data. Following, for example, McHardy et al. (2004), we will use the following bending-power-law model to fit the PSD:

$$P(f) = A f^{\alpha_L} \left[1 + \left(\frac{f}{f_b} \right)^{\alpha_L - \alpha_H} \right]^{-1}. \quad (4)$$

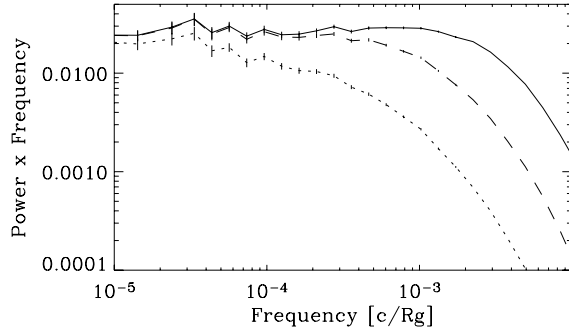


Figure 2. Filtering effect of an extended emitting region. The PSD of the variability pattern at the innermost radius, shown in the solid line, keeps a $1/f$ shape up to $f_{\text{visc}}(r_{\text{min}})$. ‘Soft’ ($\gamma = 3$) and ‘hard’ ($\gamma = 5$) light curves of the same realization, in dotted and dashed lines respectively, lose variability power at high Fourier frequencies due to the effect of the extended emitting region. For this realization, we used model parameters $Q = 0.5$, $\beta = 0$, $D = 0$.

Table 1. Bending-power-law model fits to the PSDs of simulated light curves, with emissivity indices $\gamma = 3, 4$ and 5 , for broad ($Q = 0.5$) and narrow ($Q = 10$) input signal PSDs. Higher γ values, corresponding to higher energy bands, retain more high-frequency power, evident in the flatter low-frequency slope α_L and in the higher f_b and/or flatter α_H . The fitting range used was $6 \times 10^{-5} < f < 10^{-2} c/R_g$. Note that the underlying PSDs bend continuously to steeper slopes at higher frequencies, so limiting the frequency range used for fitting, excluding higher frequencies, produces flatter slopes above the break.

	γ	α_L	$f_b (\times 10^{-3} c/R_g)$	α_H
$Q = 0.5$	3	-1.48	1.27	-3.74
	4	-1.22	1.38	-3.54
	5	-1.10	1.54	-3.46
$Q = 10$	3	-1.44	0.80	-4.73
	4	-1.16	0.96	-4.79
	5	-1.02	1.12	-4.86

Table 1 gives the values for the low- and high-frequency slopes, α_L and α_H respectively, and the break frequencies f_b that result from fitting equation (4) to PSDs with emissivity indices $\gamma = 3, 4$ and 5 , for broad ($Q = 0.5$) and narrow ($Q = 10$) input signal PSDs. These values depend slightly on the frequency range used for fitting, but reveal the general trend of more high-frequency power for harder energy bands, given by flatter α_L , and higher f_b and/or flatter α_H . Note that the underlying PSDs bend continuously to steeper slopes at higher frequencies, so limiting the frequency range used for fitting, excluding higher frequencies, produces flatter high-frequency slopes.

The emissivity indices γ also define the average traveltime of the signals as seen by the different energy bands, so they play a major role in determining the time lags. For emissivity profiles as used here, the lags show an almost power-law dependence on frequency, as can be seen in Fig. 3. This figure shows, in solid lines, the time lags between a soft light curve with $\gamma_{\text{soft}} = 3$ and hard light curves of indices $\gamma_{\text{hard}} = 3.5, 4, 5$ and ∞ , calculated for $Q = 10$. Obviously, this last light curve, taken to be the variability pattern at r_{min} , marks the limiting lag spectrum that can be obtained by increasing γ_{hard} , assuming the other parameters are fixed at the values given above. The approximate slope of these lag spectra in

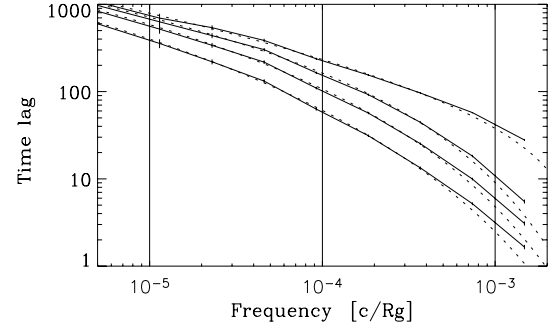


Figure 3. Time lags as a function of Fourier frequency, between a soft light curve of emissivity index $\gamma = 3$ and hard light curves of indices $\gamma = 3.5, 4, 5$ and ∞ , for $Q = 10$. Larger lags correspond to bigger differences between emissivity indices. The points joint by solid lines represent the values calculated from numerical realizations of the light curves and the dotted lines represent the lags predicted by equation (3) using the corresponding model parameters. The vertical lines mark the frequencies that will be used in the following two figures to measure lags.

the range 10^{-5} – $10^{-4} c/R_g$ goes from -0.8 for $\gamma_{\text{hard}} = 3.5$ to -0.5 for $\gamma_{\text{hard}} = \infty$.

The dotted lines in Fig. 3 are the time lags predicted by equation (3) using the parameters of the corresponding light-curve simulations. As these analytic estimates give a good fit to the simulated data, we will use them hereafter on their own or to complement the time lags calculated from simulations.

The magnitude of the time lags increases with the difference between the emissivity indices of the light curves, $\Delta\gamma = \gamma_{\text{hard}} - \gamma_{\text{soft}}$. Fig. 4 shows the fractional lags (lag \times frequency, i.e. equal to $\phi/2\pi$, where ϕ is the phase lag, see Appendix B) at the three Fourier

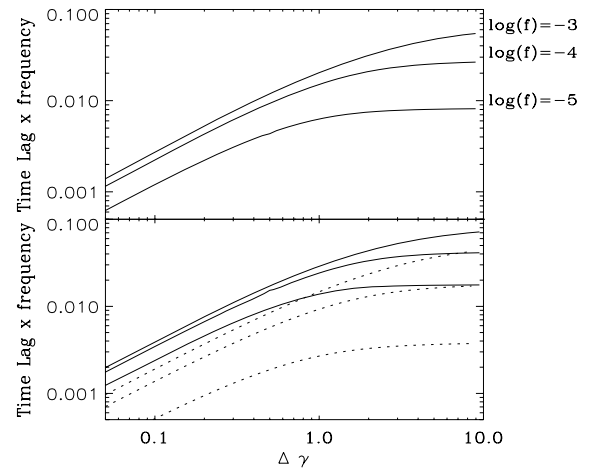


Figure 4. Top panel: fractional time lags (lags \times frequency) for energy bands of emissivity index difference $\Delta\gamma = \gamma_{\text{hard}} - \gamma_{\text{soft}}$, with $\gamma_{\text{soft}} = 3$, measured at three temporal frequencies, $f = 10^{-3}, 10^{-4}, 10^{-5} c/R_g$. The lags increase with the difference in emissivity indices and depend sensitively on this parameter up to $\Delta\gamma \sim 1$; for larger differences the lags remain at around 1–10 per cent of the Fourier frequency. As the slope of the lag spectra is greater than -1 , fractional lags are smaller at low frequencies. Bottom panel: same as above but using $\gamma_{\text{soft}} = 2.5$ (solid lines) and $\gamma_{\text{soft}} = 3.5$ (dashed lines), a steeper emissivity profile for the soft band produces smaller lags for the same difference in indices. In both panels, the lags were calculated for narrow input signal PSDs, with $Q = 10$. The value of Q affects mainly the lags at high frequencies; the lags at 10^{-5} and $10^{-4} c/R_g$ in these plots are almost independent of the Q value used.

frequencies marked in Fig. 3 by the vertical lines, $f = 10^{-3}, 10^{-4}, 10^{-5} c/R_g$, as a function of $\Delta\gamma$, calculated for a narrow input signal PSD, $Q = 10$. Each set of lines was calculated with a fixed value of γ_{soft} and varying γ_{hard} . In all cases, the lags increase rapidly with $\Delta\gamma$ up to $\Delta\gamma \sim 1$. For larger differences in emissivity indices, the lags remain at around 1–10 per cent of the variability time-scale, tending towards the limiting value obtained for $\gamma_{\text{hard}} = \infty$. In this figure, for the top panel, we used $\gamma_{\text{soft}} = 3$ and, for the bottom panel, $\gamma_{\text{soft}} = 2.5$ (solid lines) and $\gamma_{\text{soft}} = 3.5$ (dashed lines). As can be seen, for any $\Delta\gamma$, the lags increase with decreasing γ_{soft} , i.e. a more extended soft emitting region naturally produces larger lags with respect to all hard bands. Finally, the magnitude of the lags increases with decreasing frequency, but the slope of the lag spectrum is > -1 . This translates into smaller fractional lags at lower temporal frequencies.

3.2 Disc structure parameters

In our model, the product of disc structure parameters $(H/R)^2\alpha$ can be treated as a single term that governs simultaneously the characteristic frequencies of each radius and the propagation speed. We do not attempt here to model the evolution of the disc structure but only to explore the effect that varying these parameters globally has on the observable quantities. We use the prescription $(H/R)^2\alpha = Cr^{-\beta}$ to treat disc parameters that vary radially. Assuming constant α , a positive value of β implies that the accretion flow flattens outwards, approximating the case of a thin disc that expands into a thick disc or ADAF-type flow towards the centre. We have used $(H/R)^2\alpha = 0.3$ at r_{min} . Assuming $\alpha = 0.3$, this corresponds to a geometrically thick disc. The motivation for assuming this large value for $(H/R)^2\alpha$ is the need to maximize the characteristic frequencies of the innermost input signals, as the data can show significant variability up to the orbital time-scale of the last stable orbit.

Varying β changes the spacing of the radii that correspond to independent characteristic frequencies, but not the spacing of the frequencies themselves. The variability pattern at each independent annulus is not affected, but the position of each annulus in the disc shifts. Therefore, the final light curves are affected only through the effects of the extended emitting region, as the emissivity of each annulus and the traveltime between them changes. The overall effect on the PSDs is a small decrease in power towards high frequencies, produced by a steeper low-frequency PSD slope (see Table 2).

The amplitude of the time lags remains approximately unchanged, for the frequency range studied (10^{-3} – $10^{-5} c/R_g$), but the slope of the lag spectra steepens. For $\beta = 1$ and $\gamma_{\text{soft}} = 3$, the lag spectrum slope in the frequency range 10^{-5} – $10^{-4} c/R_g$ goes from -1.0 for

Table 2. Low Fourier frequency slopes, α_L , fit to PSDs of light curves generated with damping coefficients D and radial dependence of the disc parameters given by β as described in the text, for emissivity indices $\gamma = 3, 4$ and 5 . The fits are carried out only for data below $f = -3 \times 10^{-4} c/R_g$.

Model	D	β	α_L		
			$\gamma = 3$	$\gamma = 4$	$\gamma = 5$
1	2	0	−0.98	−0.83	−0.80
2	2	1	−1.19	−0.99	−0.90
3	1	0	−1.04	−0.89	−0.86
4	1	1	−1.24	−1.04	−0.95
5	0.5	0	−1.09	−0.94	−0.90
6	0.5	1	−1.26	−1.07	−0.98
7	0	0	−1.14	−1.00	−0.96
8	0	1	−1.29	−1.10	−1.02

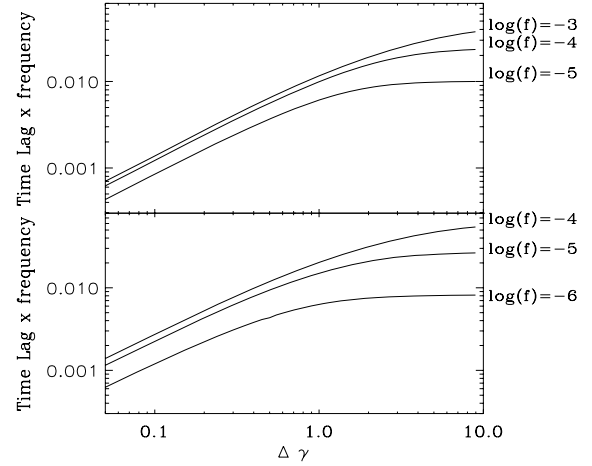


Figure 5. Top panel: same as top panel of Fig. 3 but using $\beta = 1$, i.e. constant $(H/R)^2\alpha$. The lags are similar to the $\beta = 0$ case but the slope of the lag spectrum is closer to -1 , so the fractional lags have approximately the same value at all Fourier frequencies. Bottom panel: same as top panel of Fig. 3 (using $\beta = 0$) but using $(H/R)^2\alpha = 0.03$. The lags are equivalent to the case with $(H/R)^2\alpha = 0.3$ (top panel in Fig. 4) but for frequencies a factor of 10 lower. In both panels, the lags were calculated for narrow input signal PSDs, with $Q = 10$.

$\gamma_{\text{hard}} = 3.5$ to -0.7 for $\gamma_{\text{hard}} = \infty$ (cf. the equivalent values for $\beta = 0$ of -0.8 and -0.5 , respectively). The top panel in Fig. 5 shows the fractional lags as a function of $\Delta\gamma$ for $\gamma_{\text{soft}} = 3$ and $\beta = 1$. Evidently, these functions are very similar to the $\beta = 0$ case shown in the top panel of Fig. 4, having only slightly lower lags at high frequencies and higher lags at low frequencies.

Changing the scaling constant C to lower values, i.e. as in a thinner disc, shifts all the time-scales up by the same factor. This effect shifts the PSD to lower frequencies without changing its shape. The lower panel in Fig. 5 shows the fractional time lags as a function of $\Delta\gamma$ for $\beta = 0$ and $(H/R)^2\alpha = 0.03$ instead of $(H/R)^2\alpha = 0.3$, used in all previous cases. The fractional lag spectrum is equivalent to the case with $(H/R)^2\alpha = 0.3$ (top panel in Fig. 4) except it is shifted down a factor of 10 in frequency, so the absolute value of the lag at a given frequency is a factor of 10 higher than for $(H/R)^2\alpha = 0.3$. However, notice that, as the PSD also shifts in frequency, the fractional lags at, for example, the break frequency remain approximately the same.

3.3 Input signals

So far, we have mainly considered light curves whose input signals have a Lorentzian PSD of quality factor $Q = 10$. As this shape is quite arbitrary, it is important to estimate the influence of the signal PSD on the observable parameters.

If the input signal PSDs are narrow, there is little variability power above $f_{\text{visc}}(r_{\text{min}})$ and the final PSD bends down sharply above this frequency, whereas broader input signal PSDs spill power up to higher frequencies making this drop less pronounced. Fig. 6 shows the PSDs of soft- and hard-light-curve pairs from two realizations with different Q values for the signal PSDs. For each emissivity index, the broad- and narrow input PSD realizations, plotted in dashed and solid lines respectively, have similar final power spectra, only differing noticeably near $f_{\text{visc}}(r_{\text{min}}) = 3 \times 10^{-3} c/R_g$. The same results are obtained from changing the signal PSD to, for example, a doubly broken power law. The $1/f$ behaviour of the low-frequency PSDs is produced by using equal rms per input signal and geometric

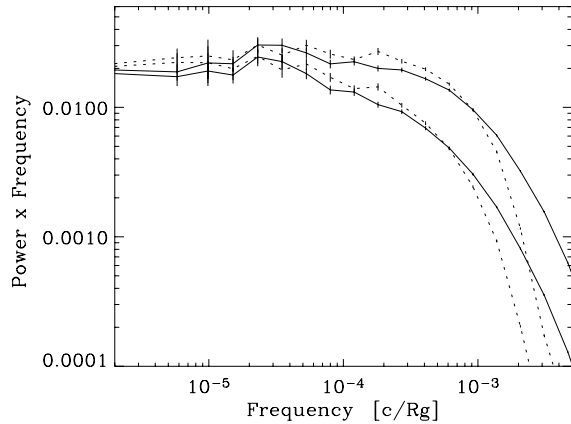


Figure 6. PSDs of soft ($\gamma = 3$, bottom) and hard ($\gamma = 4$, top), of two model realizations, with input signal PSD quality factor $Q = 0.5$ (in solid lines) and $Q = 10$ (dotted lines). The light curves with $Q = 10$ drop off more sharply than their $Q = 0.5$ counterparts close to the maximum frequency $f = 3 \times 10^{-3} c/R_g$. At lower frequencies, both realizations follow a $1/f$ relation.

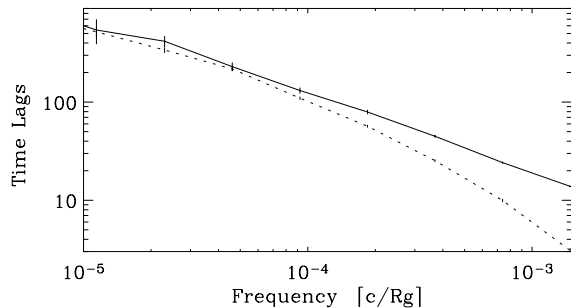


Figure 7. Time lags between soft ($\gamma = 3$) and hard ($\gamma = 4$) light curve pairs with input signal PSD quality factors $Q = 0.5$ (solid line) and $Q = 10$ (dotted line). Broader-PSD signals increase the time lags close to the maximum frequency.

separation of the signal characteristic frequencies (i.e. Lorentzian peak frequencies), and it does not depend on the shape of the signal PSDs. On the other hand, the signal PSDs define the high-frequency slope, so this part of the final PSD can serve as a diagnostic for the intrinsic variability process.

The signal PSD also affects the high-frequency end of the lag spectra. Fig. 7 shows how time lags drop off less sharply for a broad-PSD signal. At low frequencies, however, there is no evident dependence of time lag on signal PSD.

The signal PSD has a stronger effect on the coherence between two energy bands. For broad signal PSDs, a given temporal frequency will have contributions from several (incoherent) signals produced by different annuli. As the different emissivity indices highlight differing regions of the disc, the coherence between the corresponding energy bands can drop. This is shown in Fig. 8, where we plot the coherence for light curves with broad ($Q = 0.5$) and narrow ($Q = 10$) signal PSDs, using dotted and dashed lines respectively. As expected, broader signal PSDs produce a stronger drop. However, notice that in either case this loss of coherence is at most a few per cent. The emissivity indices have a much stronger effect on the coherence. For Fig. 8, we used $\gamma_{\text{soft}} = 3$ and $\gamma_{\text{hard}} = 4$. The same plot calculated for $\gamma_{\text{soft}} = 3$ and $\gamma_{\text{hard}} = 5$ would show a drop of up to 7 per cent, and for $\gamma_{\text{soft}} = 3$ and $\gamma_{\text{hard}} = \infty$, of 40 per cent, for light curves with $Q = 0.5$.

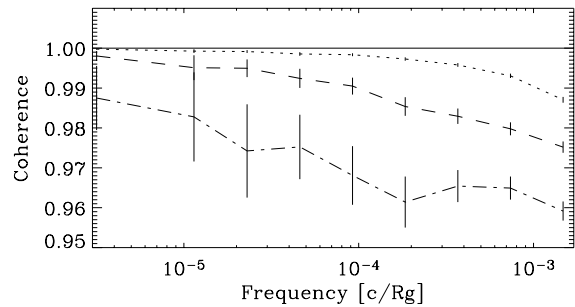


Figure 8. Coherence between soft ($\gamma = 3$) and hard ($\gamma = 4$) light curve pairs, with Lorentzian input signal PSDs with quality factors $Q = 10$ (dotted line) and $Q = 0.5$ (dashed line). The light curves with broader input signal PSDs show a stronger loss of coherence. The dot-dashed line corresponds to a $Q = 0.5$ light-curve pair affected by damping ($D = 1$), which reduces the coherence by a few extra per cent. For comparison, coherence = 1 is shown by the solid line.

3.4 Damping

The effect of damping is to reduce the amplitude of the fluctuations as they propagate inwards so that the farther they go the smaller they get. An immediate consequence is the reduction of variability power at all frequencies as seen in the PSD. As this suppression is frequency-dependent, damping can change the shape of the PSD. Fig. 9 shows the PSD for four hard light curves ($\gamma = 4$) with equal disc parameters and input signal variability amplitudes, but affected by different degrees of damping. The most noticeable change is the overall reduction of variability power. However, as the input rms is arbitrary, this effect does not help to quantify the amount of damping affecting real data. A more important effect is the change in the low-frequency slope, as damping can produce values of $\alpha_L < -1$, as seen in, for example, MCG-6-30-15 (McHardy et al. 2005). Table 2 shows the values of α_L for damping coefficients $D = 0, 0.5, 1$ and 2 , for different emissivity indices. In all cases, the stronger damping flattens the low-frequency PSD, by similar values regardless of γ , e.g. for $D = 2$ compared to $D = 0$, $\Delta\alpha_L \sim 0.17$ for $\beta = 0$ and $\Delta\alpha_L \sim 0.1$ for $\beta = 1$.

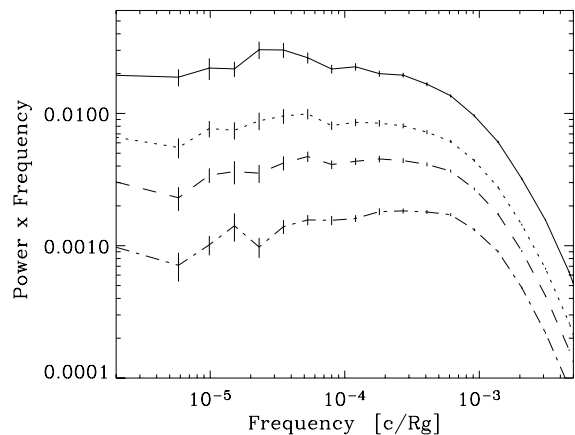


Figure 9. Effect of damping on the PSD. The solid line shows the PSD of a ($\gamma = 4$) light curve calculated without damping. The dotted, dashed and dot-dashed lines show the PSDs of similar light curves calculated with damping coefficients $D = 0.5, 1$ and 2 , respectively. Damping reduces the overall power but acts more strongly on the lowest frequencies so the low-frequency slope α_L flattens.

Damping can also reduce the coherence, especially in the case of broad input signal PSDs. The dot-dashed line in Fig. 8 shows the coherence for light curves of emissivity indices $\gamma_{\text{soft}} = 3$ and $\gamma_{\text{hard}} = 4$, $Q = 0.5$ and damping coefficient $D = 1$. These light curves only differ from those corresponding to the dashed line on the same plot by the effect of damping, which increases the loss of coherence at the highest-frequency bin from 2 to 4 per cent. Again, a larger difference in emissivity indices makes this drop more pronounced, and damping effects increase these losses accordingly: for $\gamma_{\text{soft}} = 3$ and $\gamma_{\text{hard}} = 5$, the coherence at the highest-frequency bin drops by ~ 12 per cent and, for $\gamma_{\text{soft}} = 3$ and $\gamma_{\text{hard}} = \infty$, by 60 per cent. Finally, damping can produce slightly steeper lag spectra, reducing the lags at high frequencies. This effect is small: damping coefficients of $D = 0$ and 1 produce lags differing by a factor of < 1.5 at frequencies close to the measured break frequency f_b and less at lower frequencies.

4 COMPARISON WITH AGN X-RAY LIGHT CURVES

AGN X-ray light curves from long monitoring campaigns typically show power-law PSDs with a slope ~ -1 at low frequencies, bending or breaking at high frequencies to slopes ~ -2 or steeper (e.g. Uttley, McHardy & Papadakis 2002; Markowitz et al. 2003; McHardy et al. 2004, 2005; Uttley & McHardy 2005). The high-frequency PSD is energy-dependent, with higher energy PSDs showing a higher break frequency and/or flatter slopes above the break, depending on model assumptions (e.g. McHardy et al. 2004). Significant frequency-dependent time lags have been measured in a few AGN [NGC 7469 (Papadakis et al. 2001); MCG-6-30-15 (Vaughan et al. 2003); NGC 4051 (McHardy et al. 2004); NGC 3783 (Markowitz 2005)]. In all cases, these lags increase with time-scale and energy separation of the bands and show magnitudes of up to a few per cent of the variability time-scale. The measured coherence is usually high (> 0.9) up to about the break frequency, sometimes dropping by tens of per cent above the break (Vaughan et al. 2003; McHardy et al. 2004). This behaviour is qualitatively consistent with the predictions of the fluctuating-accretion model outlined in Section 3. Now we will compare the model predictions directly to AGN data to check this consistency quantitatively.

4.1 Time lags

The time lags in NGC 4051 reported by McHardy et al. (2004) are among the largest measured in AGN, with values of ~ 0.25 , 2.5 and 4.5 per cent of the variability time-scale, when calculated between the 0.1–0.5 keV band and the 0.5–2, 2–5 and 5–10 keV bands, respectively. The slopes of the lag spectra are not well constrained but are consistent with -1 . To reproduce these large lags with the model, we chose a fairly extended soft emitting region, with emissivity index $\gamma_{\text{soft}} = 2.5$, assumed $(H/R)^2\alpha = 0.3$ at $r_{\text{min}} = 6$, used a value of $\beta = 1$ to produce a lag-spectrum slope ~ -1 and used $D = 0$. Using equation (4), we calculated the lag spectra for these model parameters, choosing emissivity indices for the remaining energy bands to match the observed lags. We used $Q = 1$ for the calculation, although other Q values produce equally good fits as the width of the input signal PSD has a very small effect in the lag spectrum over the frequency range used here (see Section 3.3). The resulting lag spectra for $\gamma_{\text{hard}} = 3.3$, 5.5 and ∞ are shown in Fig. 10, in dotted, solid and dashed lines, respectively. To convert light-crossing times to seconds, we assumed a mass of $5 \times 10^5 M_{\odot}$ (Shemmer et al. 2003). Overlaid in this figure, we show the lags

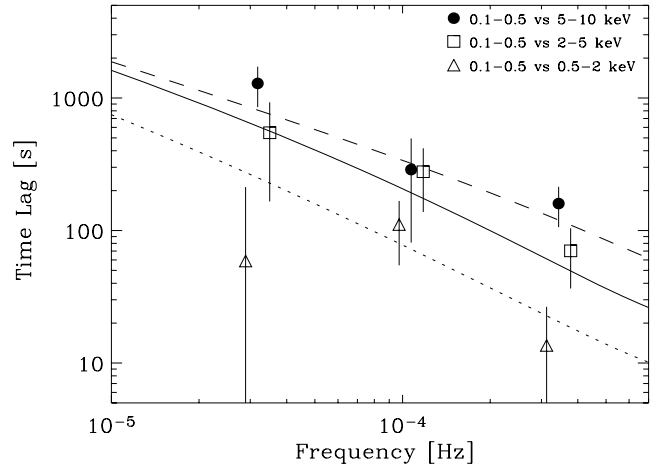


Figure 10. Time lags between the 0.1–0.5 keV band and 0.5–2, 2–5 and 5–10 keV bands (triangles, open squares and filled circles, respectively), for NGC 4051 *XMM-Newton* data. The lines represent the model lags calculated using equation (3) with model parameters fitted to match the observed PSDs as described in the text. The dotted, solid and dashed lines were calculated between synthetic light curves with emissivity indices $\gamma_{\text{soft}} = 2.5$ and $\gamma_{\text{hard}} = 3.3, 5.5$ and ∞ , and $\beta = 1$, assuming a black hole mass of $5 \times 10^5 M_{\odot}$. The filled circles are placed at the correct frequency used for the three data sets, while the squares and triangles have been shifted in this plot to slightly lower and higher frequencies respectively, to avoid overlapping the error bars.

measured from *XMM-Newton* data for NGC 4051, where the observed light curves were constructed as described in McHardy et al. (2004). Although the errors on the data are large, it is clear that the chosen model parameters are consistent with the amplitude, slope and energy dependence of the measured lags.

4.2 Energy dependence of the PSD

NGC 4051 was monitored with *RXTE* and *XMM-Newton* on long and short time-scales respectively by McHardy et al. (2004), producing a well sampled PSD over 6 decades in frequency. The high-frequency PSD in NGC 4051 shows strong energy dependence, varying from a slope $\alpha_H = 2.91 \pm 0.12$ in the 0.1–0.5 keV band to $\alpha_H = 2.06 \pm 0.16$ in the 2–5 keV band.

The difference in emissivity indices for these energy bands, suggested by the lag spectra, can also explain the energy dependence of the high-frequency PSD slope. To measure the energy dependence, we produced model light curves with broad input PSDs, $Q = 0.5$, and model parameters as described above and we fitted the final PSD with a bending-power-law model. To make a fair comparison with the data, we followed the procedure used by McHardy et al. (2004) by fixing the low-frequency slope α_L to -1.1 and the bend frequency f_b to the best-fitting value for an intermediate emissivity index, and we fitted the simulated PSDs over a similar range in frequencies. Using again $\gamma_{\text{soft}} = 2.5$ for the 0.1–0.5 keV band and $\gamma_{\text{hard}} = 5.5$ for the 2–5 keV band, we obtained PSDs that differ by $\Delta\alpha_H = -0.95$, spanning a similar range to that measured for the real data, $\Delta\alpha_{H, \text{NGC}} = -0.85 \pm 0.2$. The resulting PSDs and bending-power-law fits are shown in Fig. 11, for emissivity indices $\gamma = 2.5, 3.3$ and 5.5. Notice that, in this figure, the PSD normalizations have been rescaled to match at the low-frequency end, to highlight the different changes in slope. The filled circles in this figure correspond to $\gamma = 3.3$, which would represent the 0.5–2 keV band, as seen in Section 4.1. Correspondingly, the difference in high-frequency PSD

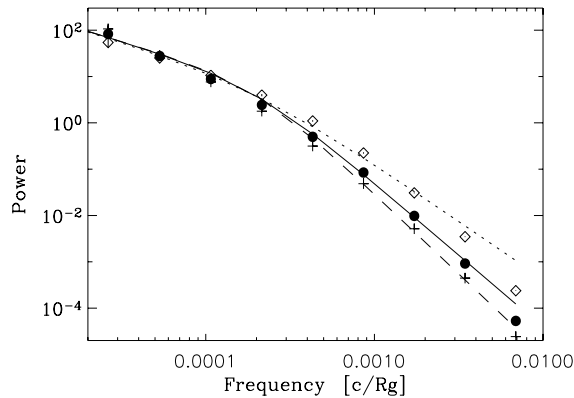


Figure 11. PSDs of three synthetic light curves of emissivity indices $\gamma = 2.5, 3.3$ and 5.5 in crosses, filled circles and open diamonds, respectively, calculated with $(H/R)^2\alpha = 0.3$, $D = 0$, $r_{\min} = 6$ and $Q = 1$. The lines mark the bending-power-law model fit to each PSD in the frequency range shown, with fixed $\alpha_L = -1.1$ and $f_b = 2 \times 10^{-4} c/R_g$. The PSD and model normalizations have been rescaled to match at the low-frequency end. The PSD of model light curves can be fitted approximately with a bending power law of fixed α_L and f_b , which highlights the differences in the high-frequency slope.

slope between the $\gamma = 2.5$ and $\gamma = 3.3$ light curves is $\Delta\alpha_H = -0.34$, placing the $\gamma = 3.3$ light curve between the 0.5 – 1.0 keV ($\Delta\alpha_{H,NGC} = -0.25$) and 1.0 – 2.0 keV ($\Delta\alpha_{H,NGC} = -0.54$) bands.

To check the consistency of the time-scales, we compared the bend frequency $f_{b,NGC}$ measured by McHardy et al. (2004), using the combined *RXTE* and *XMM-Newton* light curves, to model light curves covering a similar range in frequencies. As the NGC 4051 data used for this fit corresponded to the 4 – 10 keV *XMM-Newton* band, we used the ‘hard’ simulated light curves with γ between 5.5 and ∞ . The best-fitting bend frequencies for $\gamma = 5.5$ and ∞ , respectively, are 4.6×10^{-4} and $2 \times 10^{-3} c/R_g$. Equating these values to $f_{b,NGC} = 5 \times 10^{-4}$ Hz yields a mass of 2 – $8 \times 10^5 M_\odot$, consistent with the NGC 4051 reverberation mapping mass of $5_{-3}^{+6} \times 10^5 M_\odot$ (Shemmer et al. 2003).

A similar energy dependence of the PSD has been found in other AGN. As an example, the PSD of the Seyfert 1 galaxy MCG–6–30–15 can also be fit with a bending-power-law model obtaining flatter high-frequency slopes for higher energy light curves (Vaughan et al. 2003). The energy dependence in this case is less pronounced than in NGC 4051, possibly suggesting that the energy bands used have closer emissivity indices. Incidentally, emissivity indices that are closer in value would also produce smaller time lags, as observed in MCG–6–30–15. However, more parameters contribute to define the observed lags; for example, the mass of the central object changes the frequency range probed in terms of the light-crossing times. A comparison of the fractional lags at, for example, the PSD bend frequency in each case gives a mass-independent measure, so an extrapolation of the lag spectra in NGC 4051 published by McHardy et al. (2004) down to the break time-scale would suggest that the lags in this case are indeed systematically larger than in MCG–6–30–15.

5 APPLICATION TO CYG X-1 DATA

We now apply our simple model to data from the well-studied, persistent black hole XRB Cyg X-1, in the high/soft state.

Our model produces light curves with an $\sim 1/f$ PSD shape down to low frequencies. This is because we assume that the input signals originate at many different radii throughout the accretion disc, are

equally separated in the logarithm of frequency and have identical rms amplitudes of variability. PSDs of this shape are seen for several AGN (see previous section) and Cyg X-1 in its high/soft state.

We will use data from a short (2.3 ks) *RXTE* observation of Cyg X-1 in the high/soft state, Observation ID 10512-01-09-01, obtained on 1996 June 18.² Using proportional counter array (PCA) light curves with 2^{-8} s resolution, we measured the lag spectrum and PSD in two bands, 2 – 5.1 keV (soft band) and 8 – 13 keV (hard band). We subtracted Poisson noise, including the appropriate dead-time correction, e.g. Revnivtsev et al. (2000), before calculating the ratio of the PSDs. To keep the fitting simple, we consider only the ratio of the PSDs and not the energy-dependent PSD shapes themselves, so we do not attempt to match the PSD shape by assuming any particular input signal. This approach allows us to estimate the lags and filtering effect in a simple analytical way, by assuming that each frequency contributing to the lag spectrum and PSD ratio corresponds to a single radius, so input signal PSDs do not overlap in frequency, with the lags and PSD filtering determined using the analytical expressions given in Appendix A. We note that McHardy et al. (2004) do not claim any evidence of energy dependence of the PSD in their fitting of the same data used here, but we do find a significant energy dependence using the PSD ratio (see below). The discrepancy may result from the fact that the measured PSD ratio is, in fact, more sensitive than independent fits to the PSD, because the light curves in different bands are correlated, so that statistical scatter in the PSD due to the stochastic nature of the light curves is in the same direction in both bands, and its effect on the PSD ratio is therefore mitigated.

We first stress that, due to the complexity of fitting even our relatively simple model to the data and the difficulty of quantifying certain measurement uncertainties (see below), we will only test the broad consistency of our model with the data. Therefore, we will not quote statistical errors on parameters derived here, which should be treated as only indicative of the underlying physical parameters. Because our model contains many parameters with complex degeneracies between them, we only fit the model with a few parameters left free, to demonstrate whether the model can reproduce the data. For all our fits, we assumed a black hole mass of $10 M_\odot$. The mass provides the scaling factor between the units of light-crossing time-scale used in our method and the observed units of seconds. The effect of changing mass is therefore equivalent to that of a simple linear change in the quantity $(H/R)^2\alpha$ (see Section 3.2) at all radii and is rather weak except at high frequencies. Consistent with our earlier simulations, we initially keep $(H/R)^2\alpha = 0.3$ at all radii. We assume a fixed outer disc radius $r_{\max} = 10^5 R_g$, but allow the inner disc radius r_{\min} to vary, down to a minimum value of $1.23 R_g$ (i.e. the minimum stable orbit for a Kerr black hole). For simplicity, the soft emissivity index was initially fixed at $\gamma_{\text{soft}} = 3$, while γ_{hard} was allowed to vary. We also introduced an additional normalizing factor for the lags, so that all the lags predicted by the model can be increased by a single factor, which we leave free to vary in the fits. This renormalization represents the possibility that the fluctuations propagate at some speed proportional to the theoretically predicted local drift velocity (see Section 2.1), but not necessary equal to it.

² We do not combine data from different high/soft state observations, because there are significant variations in the timing properties in the high/soft state on time-scales of hours or longer (Cui et al. 1997; Axelsson, Borgonovo & Larsson 2005). We choose this particular observation as it is free of Lorentzian components (Cui et al. 1997) and is also fitted by McHardy et al. (2004).

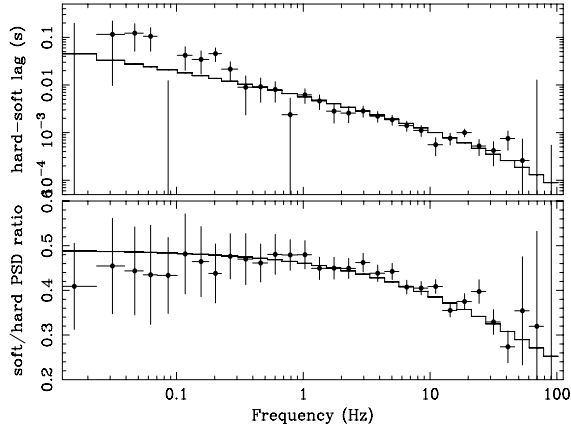


Figure 12. Time lags (top) and soft/hard PSD ratio (bottom) as a function of Fourier frequency for Cyg X-1 in the high/soft state (1996 June 18). The solid lines show the best-fitting analytical model described in the text.

Note that the PSDs in different energy bands can have different overall normalizations for a variety of reasons. For example, if a strong constant thermal emission component is present, as in the high/soft state (see Churazov et al. 2001), the variability is diluted in the soft band and the PSD normalization reduced. Alternatively, spectral pivoting at high energies (e.g. due to Compton cooling of the corona), which we do not model here, can lead to a larger normalization in the soft band compared with the hard band (e.g. see Uttley & McHardy 2005 for evidence of this effect in the AGN NGC 3227). For these reasons, when fitting our model we allow the normalization of the PSD ratio to be free.

The observed lag and soft/hard PSD ratio spectra are shown in Fig. 12, together with the best-fitting model resulting from a joint fit of the lag and filtering equations to the data, i.e. we assume the same parameters for fitting both the lag and ratio plot. The reduced chi-squared, $\chi^2/\text{d.o.f.} = 0.81$, indicates an excellent fit, for a renormalization factor of 1.86 (i.e. fluctuations propagate at ~ 1.9 times lower drift velocity than given by standard disc theory), $r_{\min} = 1.23$ and $\gamma_{\text{hard}} = 3.53$. However, we caution that the goodness-of-fit is almost certainly overestimated, because the random errors in the soft and hard PSDs are correlated at low frequencies due to the intrinsic correlation between the light curves in these bands (the correlation is much weaker at high frequencies due to Poisson noise effects), and hence the error bars at these frequencies are almost certainly overestimated. Furthermore, there is likely to be some additional uncertainty in PSD ratio at high frequencies (> 20 Hz), because an assumed Poisson noise level had to be subtracted from each PSD before the ratio was taken, and the uncertainty in the assumed noise level is not accounted for in the fit.

The small inner disc radius preferred by the data is consistent with a rapidly rotating black hole. However, this interpretation is strongly governed by our assumptions about the emissivity profile and our simplifying assumption that each frequency corresponds to a single input signal. Because the traveltime of material from $6R_g$ to $1.23R_g$ is very short, the value of r_{\min} is not driven by lags at lower frequencies, but is mainly due to a combination of the relatively large high-frequency lags and the weak drop in PSD ratio at high frequencies. Indeed, the frequencies corresponding to signals at $6R_g$ and $1.23R_g$ are 65 and 700 Hz respectively, so that, if the edge of the emitting region were observed at $6R_g$, a very pronounced drop in both the lags and the PSD ratio would be observed approaching this frequency, hence the smaller radius is preferred. However, if the

input signals overlap substantially, the larger lags from signals at larger radii can contribute even at high frequencies, so a strong drop in lag and PSD ratio would not be expected (see Section 3.3). There may also be substantial emission at radii smaller than r_{\min} , which is not considered in our model. This would also increase the lags at high frequencies and reduce the effects of filtering which cause the drop in PSD ratio at high frequencies. Thus, the small value of r_{\min} inferred from our fit is quite model-dependent and should be treated with caution.

The fact that the model can explain the soft/hard PSD ratio also implies that it can explain the results of Fourier frequency-resolved spectral analysis of the high/soft state continuum, as presented by Gilfanov, Churazov & Revnivtsev (2000). The Fourier-resolved spectra become harder at higher temporal frequencies, with the change in photon index consistent with the frequency-dependent change in PSD ratio which we measure here.

Finally, for completeness we note here that, unlike the smooth $1/f$ shape seen in the high/soft state, Cyg X-1 in the low/hard state is characterized by a band-limited PSD with a few humps, which can be modelled as four broad Lorentzian components (Pottschmidt et al. 2003). The lag spectrum also reveals a stepped structure, but it still follows approximately a $f^{-0.7}$ power-law slope. Although the model can fit reasonably well the general trend seen in the PSD ratio and lag spectra, it cannot reproduce these detailed features, indicating that some of the model assumptions are not appropriate in this case. In particular, our simple implementation of the model uses power-law emissivity indices and equal variability power per contributing annulus, so these smooth functions cannot produce additional structure at a few given frequencies. The general scheme of propagating fluctuations can still be correct but additional assumptions need to be made; for example, assuming that a few annuli have much enhanced variability power will certainly produce a bumpy PSD and might reproduce the steps in the lag spectra, as suggested by Nowak (2000) and also Kotov et al. (2001).

6 DISCUSSION

The extended emitting region in our model is responsible for the high-frequency bend in the PSD, and the associated radial emissivity profiles produce the energy dependence of the PSD and the time lags. In this section, we will summarize the spectral-timing properties produced by the model, consider the implications of the model for the size of the emitting region and discuss some possible improvements.

6.1 Time lags

Keeping the local variability time-scales tied to the propagation time-scale produces time lag spectra of power-law slope ~ -1 or flatter, and lags of ~ 1 –10 per cent of the variability time-scale, for a wide range of model parameters. As discussed in Sections 4 and 5, these simple assumptions produce lag spectra that match the data well in time-scale dependence and amplitude. We note once again that these lags arise solely due to the difference in emissivity profiles of the X-ray energy bands and do not involve any other spectral evolution of the emitting region. The amplitude of the lags depends mostly on the emissivity indices of the energy bands, increasing rapidly with their difference, up to $\Delta\gamma \sim 1$, above which the lag values tend to saturate. Significant lags can appear between energy bands characterized by similar emissivity profiles and, correspondingly, similar PSD shapes. In particular, the PSD of Cyg X-1 in the high/soft state shows weak energy dependence (see Section 5.1), but

the PSD ratio and lags can still be reproduced simultaneously with close emissivity indices for each energy band ($\Delta\gamma \sim 0.5$), provided that the propagation time-scale is slightly longer than the local fluctuation time-scale and assuming that the inner disc radius is small. The power-law shape of the lag spectra is quite robust: its slope depends only weakly on disc structure parameters $(H/R)^2\alpha$. Incidentally, the stability of the lag spectra might explain the behaviour seen in, for example, Cyg X-1, in different spectral states. This object shows very different PSD and energy spectra in the high/soft and low/hard states, indicative of different disc configurations, but surprisingly similar lags (Pottschmidt et al. 2000).

6.2 PSD shape

A comparison with AGN and BHXRB data in the high/soft state shows that the filtering effect of the extended emitting region, acting on a simple $1/f$ underlying PSD shape, can broadly reproduce their PSD shape and energy dependence. However, Cyg X-1 in the low/hard state requires a more complex *intrinsic* PSD. In either case, the extended emitting region introduces a bend in the PSD in addition to any intrinsic curvature and produces the energy dependence of the filtered PSDs.

Note that the bending power-law, used to fit AGN data, is only an approximation of the actual PSDs produced by the fluctuating-accretion model. The filtered PSD bends down continuously at high frequencies and has no well-defined high-frequency power-law slope. The difference between the bending-power-law model and the filtered PSDs can be appreciated in Fig. 11, where the single-bend PSD fit overestimates the power in the highest-frequency bins. However, as this region of the PSDs from real data is often heavily affected by Poisson noise, the associated error bars and scatter are large and it is not possible to appreciate any deviations from a simple power-law slope. Therefore, even better AGN data would be needed to discern if the model can replicate the exact PSD shape or if additional variability components are needed. We also note here that, although Revnivtsev et al. (2000) fitted the high/soft state PSD from combined data from 1996 June 4–18 with a simple power law (index -2.1) up to ~ 200 Hz, the signal-to-noise ratio at these frequencies is still fairly low and the PSD during that time is known to vary in shape between observations (Cui et al. 1997), which makes interpretation of the underlying shape even more difficult. Axelsson et al. (2005) have recently demonstrated that the high/soft state PSD can be fitted with weak Lorentzians *in addition* to a $\sim 1/f$ power-law component with an exponential cut-off. This last component is reminiscent of our simulated PSDs. Therefore, our model may be considered as representative of the times when the Lorentzians in the PSD are very weak or absent.

In our model, thick disc parameters, $\alpha(H/R)^2 = 0.3$, in the inner regions of the accretion flow and inner radius $r_{\min} = 6$ put the break frequency around 10^{-4} – $10^{-3}c/R_g$ (i.e. ~ 2 – 20 Hz for a $10 M_\odot$ black hole, 2×10^{-5} – 2×10^{-4} for a $10^6 M_\odot$). These values are in general agreement with the average break frequencies of AGN and BHXRBs, indicating that fluctuations on the viscous time-scales of a geometrically thick accretion flow are appropriate to explain the variability. A geometrically thick disc is necessary to produce the observed high-frequency fluctuations as *viscous* frequencies. If the fluctuations were instead produced on dynamical time-scales, or a magnetic time-scale related to this, as in, for example, King et al. (2004), then a thinner flow might be allowed. However, the fluctuations need not only be produced but also propagated, which poses a difficulty for much thinner accretion flows, as fluctuations on time-scales much shorter than the propagation time-scale are easily

damped (Churazov et al. 2001). Of course, this does not rule out an additional thin disc, possibly underlying the thick flow, that might contribute to the flux but not to the variability.

6.3 Extent of the emitting region

In our implementation of the variability model, the X-ray emitting region extends out to large radii. The bend in the PSD is produced by the radial distribution of variability time-scales and emissivity profiles alone and is not related to a characteristic time-scale at the maximum radius of emission. Therefore, an outer edge to the emitting region might be allowed but is not required. The steep emissivity profiles concentrate most of the emitted flux in the centre so it would make little difference to the PSD if the emitting region were truncated at some radius or if it extended out to infinity. However, the extent of the emitting region has a major impact on the lag spectra. For example, if the X-ray emission is confined to the central few R_g and responds to the variability pattern produced outside this radius, then time lags would still appear due to the radial segregation of the energy bands but, to first order, the lags would have the same value at *all* Fourier frequencies (e.g. Nowak et al. 1999b). In our case, frequency-dependent lags appear because the fluctuations are produced *within* the emitting region. This consideration gives further support to the idea that f_b does not correspond to the characteristic frequency of an outer edge of the emitting region, as noted above, as these lags are observed far below the break frequency. In turn, this implies that the X-ray emitting region should extend at least as far as the radius corresponding to the longest time-scales where frequency-dependent lags are observed.

6.4 Improvements to the model

We have made a number of simplifying assumptions that seem to reproduce the broad spectral timing properties of AGN and BHXRBs. The detailed predictions of PSDs and lag spectra can be improved by including some additional effects.

As a first step, the assumption that all radii in the disc produce the same amplitude of fluctuations can be relaxed, allowing for strongly enhanced variability at a few discrete annuli. This scenario might represent Cyg X-1 in the low/hard state where the PSD appears to be composed of a few broad Lorentzians, so it would be interesting to check if the effect of the extended emitting region would reproduce well the steps observed in the PSD ratio and in the lag spectra.

To simplify the calculations, we have only allowed for power-law radial emissivity profiles. Though this appears to be a reasonable assumption given the profile of total energy loss expected for an accretion disc, it is not clear that each energy band should follow a simple power-law profile. For example, the energy spectrum reveals other components in addition to the direct continuum that might be expected from an optically thin X-ray emitting corona. In BHXRBs in the high/soft state, blackbody disc emission is also seen, although it does not vary significantly on short time-scales (Churazov et al. 2001), so may not contribute to the observed PSD and lag spectra. However, in several AGN (e.g. NGC 4051, Uttley et al. 2004), strongly variable soft excess emission is seen below ~ 1 keV, which may be associated with Comptonized disc emission and hence could contribute a different component to the emissivity profile in the soft band. Other complex profiles might be expected. For example, by fitting the profile of the broad iron line in MCG-6-30-15 with a relativistic disc-line model, Fabian et al. (2002) have inferred a broken power-law emissivity profile, which steepens from $\gamma = 2.5$ (i.e. similar to the value we infer for NGC 4051) to $\gamma = 4.8$ within $6R_g$.

of the black hole. Thus, more complex emissivity profiles, perhaps with breaks or additional components, and taking account of general relativistic effects, could be considered. Additional variable components, arising for example through reflection or reprocessing of the primary variable emission, can also affect the coherence and time lags and should be included in more detailed variability models. In particular, in high-quality data from Cyg X-1, Kotov et al. (2001) show that a reflection component is necessary to reproduce the detailed *energy dependence* of the lags.

The simple fluctuating-accretion model presented here agrees generally well with the observational variability measurements, but still needs to be set on physical grounds to be fully validated. A physical treatment must consider two things, the source of the variability (i.e. source of accretion rate fluctuations, for example) and the source of emission. Work on the evolution of a physical (if simplified) accretion flow, implemented with numerical simulations (e.g. King et al. 2004), indicates that the necessary accretion rate fluctuations and wave-like propagation on a viscous time-scale can be realized physically. Finally, a model for the emission process and its coupling to the accretion rate fluctuations will be necessary to provide a physical motivation for the radial emissivity profiles of each energy band and, with it, a meaningful interpretation of the emissivity indices.

7 CONCLUSIONS

We have used a computational fluctuating-accretion model to reproduce the spectral-timing properties of X-ray light curves from AGN and BHXRBs. In the model, the variability is produced throughout the accretion flow as perturbations of the accretion rate on the local viscous time-scale, produced by many signals that are geometrically spaced in temporal frequency. The fluctuations propagate inwards at the radial drift velocity and modulate the fluctuations produced further in. This general scheme, introduced by Lyubarskii (1997), produces light curves that possess $1/f$ -type PSDs over a broad range of time-scales and follow a linear rms–flux relation. Following Kotov et al. (2001), X-ray emission from a radially extended region is assumed to track the local accretion rate fluctuations and to show a power-law radial emissivity profile, which steepens for higher energy bands. The different emissivity profiles and the inward propagation produce differences between the PSDs of each energy band and introduce time lags. Our implementation of the model is successful in reproducing the observed variability properties of AGN and BHXRBs, as follows.

(i) We reproduce the expected $\sim 1/f$ frequency-dependence of time lags between energy bands, and lag amplitudes of a few per cent of the variability time-scales, predicted by (Kotov et al. 2001) and observed in BHXRB and AGN variability data.

(ii) We demonstrate that the amplitudes and slopes of the lag spectra are only weakly dependent on changes in the emissivity indices, the radial dependence of the product of disc parameters $(H/R)^2\alpha$, and the strength of damping of accretion fluctuations. The robust nature of the lag spectra may help to explain the similarity of lag spectra in the low/hard and high/soft states in Cyg X-1 (Pottschmidt et al. 2000), despite the very different PSD and energy-spectral shapes in these states.

(iii) The extended emitting region suppresses short time-scale fluctuations, producing a gradual bend in the PSD at high frequencies. The ‘filtered’ PSD shapes resemble those of AGN and BHXRBs in the high/soft state (e.g. McHardy et al. 2004) and can be approximately fitted with a bending-power-law model. The bend

frequencies obtained match the observed frequencies if the fluctuations are produced on the viscous time-scales of a geometrically thick accretion flow. Values of $(H/R)^2\alpha \sim 0.3$ gave adequate bend frequencies compared to data from Seyfert galaxy NGC 4051 and the BHXRB Cyg X-1.

(iv) The fact that all energy bands are produced by the same emitting region can maintain a high coherence (>0.95) between light curves of different energy bands, as observed by, for example, Nowak et al. (1999b) and Vaughan et al. (2003). However, the coherence can be substantially reduced at high frequencies if input signals at each radius have fairly broad PSDs and the difference between emissivity profiles in different bands is large. Coherence is also reduced if damping of the inward-propagating fluctuations is significant. These results may provide an explanation for the drops in coherence observed at high frequencies in various BHXRBs and AGN (Nowak et al. 1999b; Vaughan et al. 2003; McHardy et al. 2004).

(v) The model can simultaneously reproduce both the observed energy-dependence of PSD shape and the lag spectrum for the AGN NGC 4051 and the BHXRB Cyg X-1 in the high/soft state, although the inferred propagation times in Cyg X-1 are slightly slower than the drift velocity expected for a standard disc. In the low/hard state of Cyg X-1, our simple model can reproduce the general slope of the lag spectrum but cannot account for the stepped shape of the lag spectrum. Modelling the detailed features of this spectrum would require additional assumptions about the mechanism producing the variability.

(vi) Direct comparison with spectral-timing data from AGN and BHXRBs shows good general agreement with the model. However, we note that if the model is correct, the empirical bending or broken power-law models used to fit the PSDs of AGN and BHXRBs in the high/soft state must break down for high signal-to-noise ratio data, because they only approximate the gradual bending shape predicted by our model. Also, we note that the model implies that the PSD bend time-scale measured for AGN and BHXRBs is a function of both the underlying PSD of accretion fluctuations (which can contain intrinsic breaks) and the emissivity profile of the observed energy band (which introduces a high-frequency bend). Therefore, the PSD bend time-scale is not necessarily associated with the outer radius of the emitting region, and this region can, in principle, be extremely large, provided the emissivity profile is relatively steep.

ACKNOWLEDGMENTS

This research has made use of data obtained from the High Energy Astrophysics Science Archive Research Centre (HEASARC), provided by the NASA Goddard Space Flight Center. We wish to thank the two anonymous expert referees for their valuable comments. PA acknowledges support from the International Max-Planck Research School in Astrophysics (IMPRS), travel support from grants associated with the NASA *RXTE* Guest Observer programme, and the hospitality of the NASA Goddard Space Flight Center. PU acknowledges a Research Associateship from the National Research Council.

REFERENCES

- Axelsson M., Borgonovo L., Larsson S., 2005, *A&A*, 438, 999
- Churazov E., Gilfanov M., Revnivtsev M., 2001, *MNRAS*, 321, 759
- Cui W., Zhang S. N., Focke W., Swank J. H., 1997, *ApJ*, 484, 383
- Fabian A. C. et al., 2002, *MNRAS*, 335, L1
- Gierliński M., Zdziarski A., 2003, *MNRAS*, 343, L84
- Gilfanov M., Churazov E., Revnivtsev M., 2000, *MNRAS*, 316, 923

- Kato S., Fukue J., Mineshige S., 1998, *Black-Hole Accretion Discs*. Kyoto Univ. Press, Kyoto
- King A. R., Pringle J. E., West R. G., Livio M., 2004, *MNRAS*, 348, 111
- van der Klis M., 1995, in Lewin W. H. G., van Paradijs J., van den Heuvel E. P. J., eds, *X-ray Binaries*. Cambridge Univ. Press, Cambridge, p. 252
- Kotov O., Churazov E., Gilfanov M., 2001, *MNRAS*, 327, 799
- Lyubarskii Y. E., 1997, *MNRAS*, 292, 679
- McHardy I. M., Papadakis I. E., Uttley P., Page M. J., Mason K. O., 2004, *MNRAS*, 348, 783
- McHardy I. M., Gunn K. F., Uttley P., Goad M. R., 2005, *MNRAS*, 359, 1469
- Markowitz A., 2005, *ApJ*, 635, 180
- Markowitz A. et al., 2003, *ApJ*, 593, 96
- Miyamoto S., Kitamoto S., 1989, *Nat*, 342, 773
- Narayan R., Yi I., 1994, *ApJ*, L13
- Nowak M. A., 2000, *MNRAS*, 318, 361
- Nowak M. A., Wilms J., Dove J. B., 1999a, *ApJ*, 517, 355
- Nowak M. A., Vaughan B. A., Wilms J., Dove J. B., Begelman M. C., 1999b, *ApJ*, 510, 874
- Papadakis I. E., Nandra K., Kazanas D., 2001, *ApJ*, 554, 133
- Pottschmidt K., Wilms J., Nowak M. A., Heindl W. A., Smith D. M., Staubert R., 2000, *A&A*, 357, 17
- Pottschmidt K. et al., 2003, *A&A*, 407, 1039
- Press W. H., Teukolsky S. A., Vetterling W. T., Flannery B. P., 1992, *Numerical Recipes*. Cambridge Univ. Press, Cambridge
- Reig P., Papadakis I., Kylafis N. D., 2002, *A&A*, 382, 202
- Revnivtsev M., Gilfanov M., Churazov E., 2000, *A&A*, 363, 1013
- Shakura N. I., Sunyaev R., 1973, *A&A*, 24, 337
- Shemmer P., Uttley P., Netzer H., McHardy I. M., 2003, *MNRAS*, 343, 1341
- Timmer J., König M., 1995, *A&A*, 300, 707
- Uttley P., 2004, *MNRAS*, 347, 61
- Uttley P., McHardy I. M., 2001, *MNRAS*, 323, 26
- Uttley P., McHardy I. M., 2005, *MNRAS*, 363, 586
- Uttley P., McHardy I. M., Papadakis I. E., 2002, *MNRAS*, 332, 231
- Uttley P., Taylor R. D., McHardy I. M., Page M. J., Mason K. O., Lamer G., Fruscione A., 2004, *MNRAS*, 347, 1345
- Uttley P., McHardy I. M., Vaughan S., 2005, *MNRAS*, 359, 345
- Vaughan B., Nowak M., 1997, *ApJ*, 474, L43
- Vaughan S., Fabian A. C., Nandra K., 2003, *MNRAS*, 339, 1237

APPENDIX A: ANALYTICAL ESTIMATES FOR FILTERED PSD AND LAGS

As mentioned in Section 2, the extended emitting region acts as a low-pass filter on the PSD. This filter factor, F , can be approximated as

$$\text{PSD}_{\text{filt}}(f) = \text{PSD}(f) \times F(r_f) = \text{PSD}(f) \left[\frac{\int_{r_{\min}}^{r_f} \epsilon(r) 2\pi r dr}{\int_{r_{\min}}^{\infty} \epsilon(r) 2\pi r dr} \right]^2. \quad (\text{A1})$$

Taking the emissivity profile $\epsilon(r) = r^{-\gamma} (1 - \sqrt{r_{\min}/r})$, the filter factor takes the form (for $\gamma > 2$)

$$F(r_f) = \left(\frac{\frac{r_f^{2-\gamma} - r_{\min}^{2-\gamma}}{2-\gamma} - \sqrt{r_{\min}} \frac{r_f^{1.5-\gamma} - r_{\min}^{1.5-\gamma}}{1.5-\gamma}}{\frac{r_{\min}^{2-\gamma}}{\gamma-2} + \frac{r_{\min}^{2-\gamma}}{1.5-\gamma}} \right)^2 = \left\{ 1 - \frac{2r_f^{2-\gamma}}{r_{\min}^{2-\gamma}} \left[\gamma - 1.5 - \sqrt{\frac{r_{\min}}{r_f}} (\gamma - 2) \right] \right\}^2. \quad (\text{A2})$$

In our implementation, the fluctuations are produced on the viscous time-scale at the radius of origin, so $r_f = [2\pi f (R/H)^2 / \alpha]^{-2/3}$. Substituting this value in the equation above gives the PSD filtering factor as a function of frequency f , where f is in units of c/R_g . This approximation for the filtering effect is appropriate for narrow input PSD signals, where most of the variability power produced by each annulus is produced on the corresponding viscous time-scale. Finite traveltimes effects contribute to cancel out variability produced at higher frequencies than f_{visc} , so the filtered PSD in this case is distorted further.

For the calculation of the time lags, the average traveltimes of a signal produced at r_s can be approximated as

$$\bar{\tau}(s) = \frac{\int_{r_{\min}}^{r_s} \tau(r, r_s) \epsilon(r) 2\pi r dr}{\int_{r_{\min}}^{r_s} \epsilon(r) 2\pi r dr}, \quad \tau(r, r_s) = \int_r^{r_s} \frac{d\tilde{r}}{v(\tilde{r})}. \quad (\text{A3})$$

If the fluctuations propagate with viscous velocity, $v(r) = \alpha(H/R)^2 r^{-1/2}$, then $\tau(r, r_s) = \frac{2}{3\alpha(H/R)^2} (r_s^{3/2} - r^{3/2})$ and the average traveltimes can be calculated using the emissivity profile given above. For example, for the case where $\gamma \neq 1.5, 2, 3, 3.5$, the average traveltimes is

$$\bar{\tau}(s) = \frac{\left[\frac{2}{3\alpha(H/R)^2} \left(r_s^{1.5} \frac{r_s^{2-\gamma} - r_{\min}^{2-\gamma}}{2-\gamma} - r_s^{1.5} r_{\min}^{0.5} \frac{r_s^{1.5-\gamma} - r_{\min}^{1.5-\gamma}}{1.5-\gamma} - \frac{r_s^{3.5-\gamma} - r_{\min}^{3.5-\gamma}}{3.5-\gamma} + r_{\min}^{0.5} \frac{r_s^{3-\gamma} - r_{\min}^{3-\gamma}}{3-\gamma} \right) \right]}{\left(\frac{r_s^{2-\gamma} - r_{\min}^{2-\gamma}}{2-\gamma} - r_{\min}^{0.5} \frac{r_s^{1.5-\gamma} - r_{\min}^{1.5-\gamma}}{1.5-\gamma} \right)} \quad (\text{A4})$$

Substitution of the exponentials with logarithms in the appropriate terms gives the equation for the rest of the cases. For signals produced on the viscous time-scale of the radius of origin, r_s can be substituted by r_f as above, producing average traveltimes as a function of temporal frequency. Finally, the difference between $\bar{\tau}(f)$ calculated for two different emissivity indices γ gives the time lag spectrum corresponding to this γ pair.

APPENDIX B: SPECTRAL-TIMING MEASUREMENTS

We estimate the PSD using the periodogram, where the variability power, $P(f_i)$, is calculated for discretely sampled frequencies f_i as

$$P(f_i) = \frac{2}{\bar{s}^2} \frac{\Delta t}{N} \left| \text{Re}_s^2(f_i) + \text{Im}_s^2(f_i) \right|, \quad (\text{B1})$$

where $\text{Re}_s(f_i)$ and $\text{Im}_s(f_i)$ are the real and imaginary parts of the discrete Fourier transform of the time series $s(t)$, \bar{s} is the average count rate, Δt is the sampling time interval and N is the number of sampled points (Press et al. 1992).

The cross-spectrum between two time series, e.g. simultaneous soft and hard light curves, $s(t)$ and $h(t)$, is defined as $C(f) = S^*(f)H(f)$, where $S(f)$ and $H(f)$ are the Fourier transforms of the respective light curves. The cross-spectrum is a complex-valued function, from where the coherence and phase lags can be extracted. The coherence γ^2 for discretely sampled time series is calculated as

$$\gamma^2(f_i) = \frac{\langle \text{Re}_C(f_i) \rangle^2 + \langle \text{Im}_C(f_i) \rangle^2}{\langle |S(f_i)|^2 \rangle \langle |H(f_i)|^2 \rangle}, \quad (\text{B2})$$

where $\text{Re}_C(f_i)$ and $\text{Im}_C(f_i)$ are the real and imaginary parts of the cross-spectrum $C(f)$ and angle brackets represent averaging over independent measurements (i.e. the numerator in the equation is the modulus-squared of the averaged cross-spectrum). Note that here, the averaging of independent measurements of the cross-spectrum and PSD is carried out by binning up in frequency, as well as by averaging measurements of the cross-spectrum measured at the same frequency from separate light-curve segments.

The argument of the cross-spectrum defines the phase lags, $\phi(f_i) = \arg \langle C(f_i) \rangle$, and from here the time lags, $\tau(f_i)$, are calculated as

$$\tau(f_i) = \frac{\phi(f_i)}{2\pi f_i} = \frac{1}{2\pi f_i} \arctan \left[\frac{\langle \text{Im}_C(f_i) \rangle}{\langle \text{Re}_C(f_i) \rangle} \right]. \quad (\text{B3})$$

For a more detailed discussion on the measurement and interpretation of coherence and time lags, and the determination of errors on these measurements, see Vaughan & Nowak (1997), Nowak et al. (1999b) and, in the context of AGN, Vaughan et al. (2003).

This paper has been typeset from a \LaTeX file prepared by the author.